Research Article Vol. 4, No. 3 / 25 June 2026 / Optica Quantum 305

OPTICA QUANTUM

Narrowband frequency-entangled photon source for Hong–Ou–Mandel interferometry

YEN-JU CHEN,[1,2,*] SHENG-HSUAN HUANG,[1,2] THOMAS DIRMEIER,[1,2] KAISA LAIHO,[3] DMITRY V. STREKALOV,[2] ANDREA AIELLO,[2] GERD LEUCHS,[1,2] AND CHRISTOPH MARQUARDT[1,2]

[1]Department of Physics, Friedrich-Alexander-Universität Erlangen-Nürnberg, Staudtstrasse 7/A3, 91058 Erlangen, Germany
[2]Max Planck Institute for the Science of Light, Staudtstrasse 2, 91058 Erlangen, Germany
[3]German Aerospace Center (DLR e.V.), Institute of Quantum Technologies, Wihelm-Runge-Str. 10, 89081 Ulm, Germany
*yen-ju.chen@fau.de

Received 2 March 2026; revised 5 May 2026; accepted 8 May 2026; published 23 June 2026

Hong–Ou–Mandel (HOM) interferometry with entangled photons exhibits distinctive quantum features. By introducing frequency entanglement (discrete-color entangled states) into HOM interference, the characteristic HOM dip is modulated by sinusoidal fringes, which significantly enhances the sensitivity of HOM sensors. The frequency-entangled photon sources demonstrated to date rely on non-resonant parametric down-conversion (PDC), which limits the photon coherence length and, consequently, restricts the sensing dynamic range to the millimeter scale. In this work, we demonstrate narrowband frequency-entangled photon source based on resonant PDC in a crystalline whispering gallery mode resonator. The MHz-level spectral bandwidth of photons enables a meter-scale dynamic range. With highly nondegenerate frequency-entangled photon pairs featuring a 96 THz frequency detuning, we observe high-contrast quantum beating with sub-picosecond resolution in the HOM experiment. Our WGMR-based frequency-entangled photon source has potential applications in quantum metrology and quantum information processing.

https://doi.org/10.1364/OPTICAQ.596595

1. INTRODUCTION

Hong–Ou–Mandel (HOM) interferometry has emerged as a useful tool for the development of novel quantum sensing techniques, with applications ranging from quantum optical coherence tomography [1], quantum microscopy [2], entangled-photon spectroscopy [3], to quantum gyroscopy [4]. Interestingly, when frequency-entangled photon pairs, where the photons are entangled across two well-separated frequency modes, are used in HOM interference, the resulting interference pattern exhibits a characteristic HOM dip modulated by sinusoidal fringes. Here, the beating period of the fringes corresponds to the frequency difference between the two entangled photons [5–8]. The optical time delay information can then be extracted from the fringe phase rather than the HOM dip position, thus significantly increasing the measurement resolution. Leveraging this enhanced information per photon, the quantum beat note reduces the acquisition time required to achieve high-resolution sensing. Utilizing frequency-entangled photon pairs, a fast HOM sensor with nanometer-scale resolution and second-scale acquisition time was reported in [8], demonstrating the potential of entanglement-based HOM sensor for real-time quantum sensing.

To date, frequency-entangled photon source has been realized in Sagnac loop [7,9] and two-crystal configuration [6,8]. Although previous approaches have achieved frequency detuning up to 177 THz, the relatively broad photon bandwidths (≈0.5 nm) correspond to coherence times of only a few picoseconds, limiting the dynamic range of HOM sensor to the millimeter scale. Moreover, the broad spectral bandwidth of photons generated in bulk nonlinear media poses challenges for efficient light–matter interactions, such as atomic quantum memories, which typically require MHz-level bandwidths [10,11].

To overcome the coherence time and spectral bandwidth limitations, resonant parametric down-conversion (PDC) provides a powerful approach to generate narrowband photon pairs with significantly extended temporal coherence. While achieving multi-resonance conditions under large frequency detuning in resonant PDC is generally challenging, whispering gallery mode resonators (WGMRs) offer a particularly advantageous platform [12–14]. Taking advantage of the total internal reflection of light within the WGMR, the triple resonance of pump, signal, and idler fields at significantly different wavelengths can be naturally supported without the need for complex reflector fabrication or active cavity control.

In this work, we demonstrate a narrowband frequency-entangled photon source based on PDC in a crystalline WGMR. Using highly nondegenerate frequency-entangled photon pairs with a frequency detuning of 96 THz, we observed high-contrast HOM interference fringes with sub-picosecond resolution over the wide photon coherence length. The MHz-level spectral bandwidth enables a significantly extended dynamic range reaching the meter scale. This long dynamic range relaxes the requirement for precise alignment of the interferometer paths, which may have advantages for long-baseline measurements [15]. Our WGMR-based entangled photon source may have potential applications in the study of entangled light–matter interactions and quantum metrology.

2. THEORETICAL DESCRIPTION

The frequency-entangled state can be described as

$$|\psi\rangle = \frac{1}{\sqrt{2}} \iint dtdt' e^{-i(\omega_s t+\omega_i t')} \phi(t-t')[a^{\dagger}_{sA}(t)a^{\dagger}_{iB}(t') + a^{\dagger}_{sB}(t)a^{\dagger}_{iA}(t')]|0\rangle, \quad (1)$$

where $\phi(t-t')$ is the wave-packet temporal profile of photon pair. The bosonic operator creating a signal (idler) photon at time t in the input port A (B) of the HOM interferometer is denoted as $a^{\dagger}_{sA(iB)}(t)$. The angular frequencies of the signal and idler photons are denoted as ω_s and ω_i, respectively. After the 50/50 beam-splitter transformation, the Glauber correlation function between the two output ports, mode C and D, is calculated as

$$G^{(2)}(\tau) = \langle a^{\dagger}_C(t_0+\tau)a^{\dagger}_D(t_0)a_D(t_0)a_C(t_0+\tau)\rangle. \quad (2)$$

By integrating the Glauber correlation function over the coincidence window, the coincidence detection probability as a function of the time difference τ between the photons arriving at the two output ports can be expressed as

$$P_c = \frac{1}{2}\left[1 - V\int d\tau\phi(\tau+\Delta t)\phi(\tau-\Delta t)\cos(\Delta\omega\Delta t)\right], \quad (3)$$

where V is the interference visibility. The relative time delay between the two arms of the interferometer is denoted as Δt. The angular frequency detuning between the signal and idler is defined as $\Delta\omega = \omega_s - \omega_i$. In the resonant PDC case, the wave packet of the photon pair in the time domain can be described by a double-exponential decay function [16]:

$$\phi(t_s - t_i) = \sqrt{\frac{2\Gamma_s\Gamma_i}{\Gamma_s+\Gamma_i}} \times \begin{cases} e^{-\Gamma_s(t_s-t_i)}, & t_s - t_i \geq 0, \\ e^{\Gamma_i(t_s-t_i)}, & t_s - t_i < 0, \end{cases} \quad (4)$$

where Γ_s and Γ_i are the decay rate of the cavity in the signal and idler modes, respectively. The calculated HOM interference patterns for various frequency detuning between the signal and idler photons are shown in Fig. 1(a). In the degenerate case, the interference exhibits a characteristic HOM dip, whose width scales with the coherence time of the photon pairs. This broad HOM dip limits the temporal resolution for time-resolved detection applications. As the frequency detuning between the signal and idler photons increases, the resulting HOM dip is modulated by sinusoidal fringes, with a fringe period inversely proportional to the frequency detuning between the two photons. This modulation transforms the broad HOM dip into a finely structured interference pattern, which is highly sensitive to changes in relative time delay. The temporal resolution of the time-delay measurement is thus significantly enhanced. The time-delay information extracted from the HOM interference can be evaluated by analyzing the Fisher information (FI). Considering negligible photon loss, the FI at relative time delay Δt can be written as [6,17]

$$F = \frac{[\partial_{\Delta t}P_c(\Delta t)]^2}{P_c(\Delta t)} + \frac{[\partial_{\Delta t}P_a(\Delta t)]^2}{P_a(\Delta t)} = \frac{[\partial_{\Delta t}P_c(\Delta t)]^2}{P_c(\Delta t)[1-P_c(\Delta t)]}, \quad (5)$$

where $P_a = 1 - P_c$ denotes the detection probability of anti-coincidence events. The calculated FI is shown in Fig. 1(b). As the FI scales quadratically with the frequency detuning between the signal and idler photons, the measurement precision can be substantially improved when using highly nondegenerate frequency-entangled photon pairs (see Supplement 1 for more

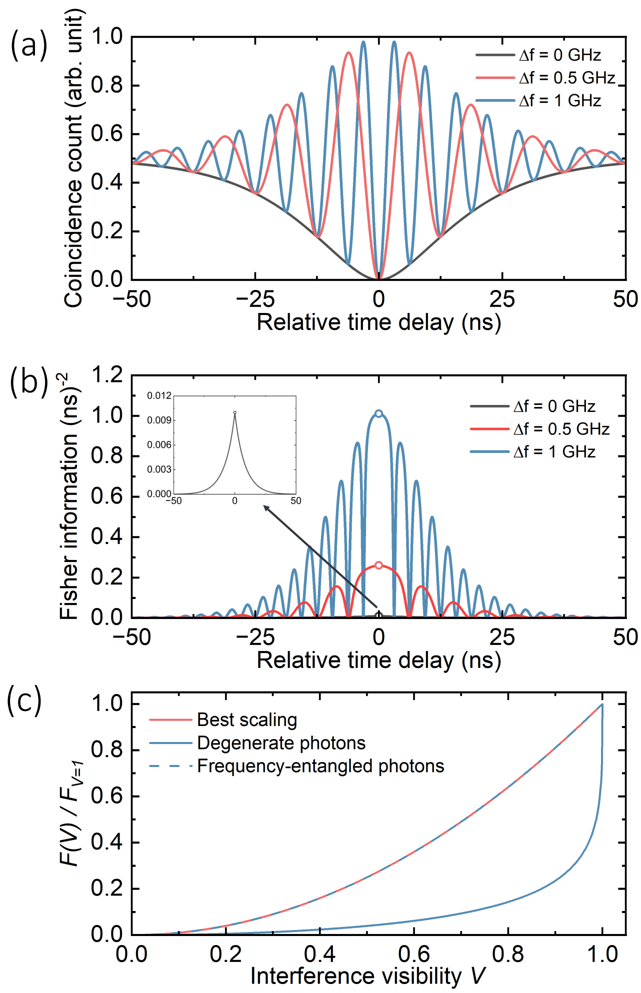

Fig. 1. (a) HOM interference of frequency-entangled photons and the corresponding (b) Fisher information for various frequency detuning between the signal and idler photons $\Delta f = \Delta\omega/2\pi$. The open circle represents the point where the Fisher information is undefined. The inset shows an enlarge view of the Fisher information calculated with degenerate photon pairs. The interference visibility in the calculations is $V = 1$. (c) Fisher information ratio as a function of interference visibility. The angular frequency detuning between the signal and idler photons for frequency-entangled state is $\Delta\omega = 10$ THz. The best scaling refers to the optimal quadratic dependence of the Fisher information on visibility [16]. In the calculations, the waveform of the state is double-exponential decay function with cavity decay rates $\Gamma_s = \Gamma_i = 1/20\ \mathrm{ns}^{-1}$.

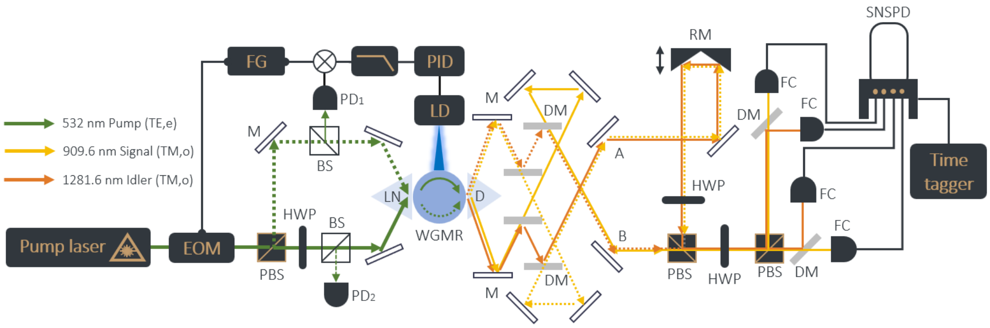

Fig. 2. Schematic of the experimental setup. The solid and dashed lines represent the beams coupled into and out of the resonator in the clockwise and counterclockwise directions, respectively. BS, non-polarizing beam splitter; D, diamond prism; DM, dichroic mirror; EOM, electro-optic modulator; FC, fiber collimator; FG, function generator; HWP, half-wave plate; LD, laser diode; LN, x-cut $LiNbO_3$ prism; M, mirror; PBS, polarizing beam splitter; PD, photodetector; PID, proportional–integral–derivative controller; RM, retroreflector mirror; SNSPD, superconducting nanowire single-photon detector; TE, transverse electric modes; TM, transverse magnetic modes; WGMR, whispering gallery mode resonator; o, ordinary; and e, extraordinary.

details). Additionally, the use of narrowband photon pairs leads to a broader temporal wave-packet, which corresponds to an extended sensing range due to the increased photon coherence time.

In the ideal case, the FI from the perfect HOM interference saturates the QCR limit. In practice, however, the precision of a HOM sensor is limited by imperfect interference visibility, which significantly reduces the attainable FI. In this scenario, the waveform of the state, which is related to its effective occupation area in the time-frequency phase space, offers an alternative way to improve the measurement precision. As shown in Fig. 1(c), for degenerate photon pairs with a double-exponential decay waveform, the ratio of the maximal achievable FI at non-ideal visibility to its ideal value falls to 0.5 when the visibility is reduced to 0.98. Remarkably, as reported in Ref. [18], the frequency-entangled state shows robust precision improvements against the reduced visibility and saturates the best scaling of the FI ratio, which scales quadratically with the visibility $F(V) = V^2 F_{V=1}$. Without the need for additional spectral mode engineering, the frequency-entangled state exhibits sinusoidal characteristics in its chronocyclic Wigner function similar to those of a Schrödinger-cat-like state, rendering the frequency-entangled state inherently more resilient to visibility imperfections [18,19].

3. EXPERIMENTAL SETUP AND RESULTS

The schematic of the experimental setup is shown in Fig. 2. Our WGMR is made of z-cut 5% MgO-doped lithium niobate ($LiNbO_3$) with a resonator radius $R \approx 0.745$ mm and a rim radius $r \approx 0.144$ mm. The temperature of the WGMR is stabilized at 22.5 °C to satisfy type-I phase-matching condition, with the pump, signal, and idler wavelengths at 532 nm, 909.6 nm, and 1281.6 nm, respectively. By shining a 462 nm heating laser onto the WGMR, the resonator temperature is further fine-tuned to lock the pump mode resonant frequency to the pump laser frequency based on the Pound–Drever–Hall (PDH) technique. The WGMR is pumped with a continuous-wave frequency-doubled Nd:YAG laser from the clockwise (CW) and counterclockwise (CCW) directions via an x-cut $LiNbO_3$ prism. Non-polarizing beam splitters are used to extract the reflected beams, which are then measured with photodiodes as the pump laser frequency is scanned to obtain the reflectance spectra. The pump laser is

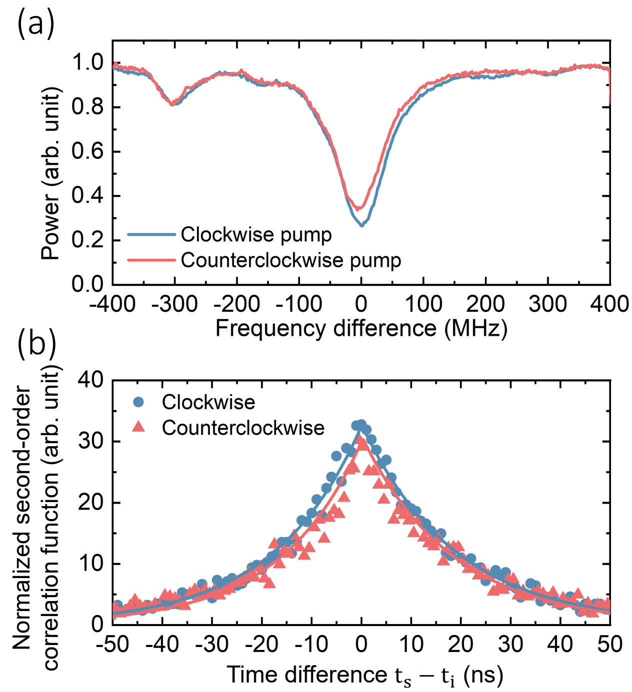

Fig. 3. (a) Reflectance spectra for the pump beams in the CW and CCW directions measured from photodetectors D_1 and D_2, respectively. (b) Normalized second-order correlation functions of photon pairs generated in the CW and CCW directions of the WGMR.

aligned to couple into the fundamental resonant mode, for which the radial and the angular mode numbers are $q_p = 1$ and $p_p = 0$, respectively [20]. To ensure that the pump beams from two directions are coupled to the same resonant mode, both beams are aligned to produce the same reflected spectra, and the reflectance is optimized to maximize the pump power coupled into the desired resonant mode by matching the spatial overlap between the pump WGM geometric profile and the pump beam, and by adjusting the incidence angle of the latter. The reflectance spectra for the pump in the CW and CCW directions are shown in Fig. 3(a). The measured bandwidth is 99.1 MHz, corresponding to a quality factor (Q) of 5.7×10^6.

The generated signal and idler photons are coupled out by a diamond prism. To achieve a higher nondegeneracy of the photon pairs at room temperature, the signal photon is excited in the fundamental mode ($q_s = 1, p_s = 0$), whereas the idler photon is excited in a higher-order radial mode ($q_i = 2, p_i = 0$) [20]. These highly nondegenerate photon pairs are first separated by a dichroic mirror (DM). The signal and idler photons from the CCW mode are then directed to paths A and B, respectively, generating the state $|\omega_s\rangle_A|\omega_i\rangle_B$. Conversely, the signal and idler photons from the CW mode are routed to paths B and A, producing $|\omega_i\rangle_A|\omega_s\rangle_B$. In this way, the frequency-entangled state (1) is prepared. After the entangled state preparation, the beams are recombined into the same path with orthogonal polarization modes by using a half-wave plate (HWP) and a polarizing beam splitter (PBS). The HOM interference can then be efficiently implemented by applying a diagonal polarization transformation with a HWP, followed by beam separation using a PBS. After the interference, a DM with a 1000 nm cut-off wavelength is used to separate the signal and idler photons prior to detection. Under destructive interference, the coincidence count can only be measured between the detectors located at the same output port of the PBS. Note that the pump laser coupled out of the WGMR is filtered out by using bandpass filters before the fiber collimators (not shown in the figure) to suppress accidental coincidence counts.

The measured Glauber correlation functions of the photon pairs generated in CW and CCW modes are shown in Fig. 3(b). The cavity decay rates of the signal and idler photons are $\Gamma_s = 1/(18.84 \pm 0.35)\ \mathrm{ns}^{-1}$ and $\Gamma_i = 1/(17.53 \pm 0.33)\ \mathrm{ns}^{-1}$, corresponding to single-photon bandwidths of (8.45 ± 0.16) MHz and (9.08 ± 0.17) MHz, respectively. The bandwidth of photon pairs can be calculated as $\Delta\Omega = [(\sqrt{\Gamma_s^4 + 6\Gamma_s^2\Gamma_i^2 + \Gamma_i^4} - \Gamma_s^2 - \Gamma_i^2)/2]^{1/2}$, yielding a photon-pair bandwidth of (5.63 ± 0.07) MHz [16]. This high-Q WGMR enables a detection rate of the frequency-entangled photons of 1.1×10^6 pairs per second per mW pump power.

To probe the HOM interference properties of the frequency-entangled photon pairs, a retroreflector mirror (RM) mounted on a high-precision motorized translation stage with a travel range of 70 mm is employed to introduce a controllable optical path delay between the two arms of the HOM interferometer. The coarse optical path delay is introduced by first positioning the RM at the desired set point. The RM is then continuously translated in 0.1 μm increments to finely scan the HOM fringes. By summing the coincidence counts between two output ports of the interferometer within a coincidence window (±50 ns), the measured coincidence count exhibits sinusoidal oscillations [Fig. 4(a)]. The fitted beating period is $(3.08 \pm 0.01))$ μm, which is close to the expected period of (3.134 ± 0.002) μm calculated from the (95.58 ± 0.05) THz frequency detuning between the signal (909.6 ± 0.1) nm and idler photons (1281.6 ± 0.3) nm. The interference visibility is (87.3 ± 2.6) %, which can be further improved by reducing the pump power [21]. Lowering the pump power suppresses the probability of multi-pair generation and ensures operation within the low-gain regime (with our OPO threshold of approximately 4 μW). As a result, the peak value of the signal–idler cross-correlation function $g_{si}^{(2)}(0)$ is enhanced, leading to improved interference visibility. Due to the long coherence length of the photon pairs, our HOM interferometer does not require precise initial calibration of the relative optical path delay to observe the HOM interference pattern. Moreover, the broad temporal region with nonzero interference visibility provides a wide dynamic range for sensing

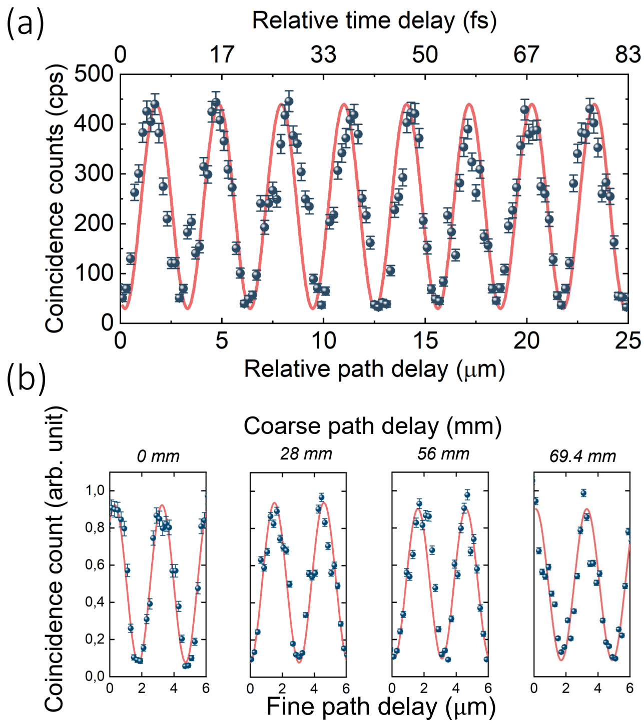

Fig. 4. (a) HOM interference of narrowband frequency-entangled photons. The highest interference visibility achieved is (87.3 ± 2.6) % based on the best fit (red curve). (b) HOM interference with various optical path delays. The HOM interference fringes are measured under critical coupling conditions, where the coupling rate is approximately equal to the internal loss rate. Under these conditions, the photon-pair bandwidth is approximately (5.63 ± 0.07) MHz. The red curves are the best fit to the measured data. The errors are calculated assuming Poissonian statistics for photon counting. The experiments were performed with a pump power of 150 nW for each pump beam in the CW and CCW directions. The OPO threshold is approximately 4 μW.

applications, where the absolute distance measurement can be performed by counting the fringes in a manner of vernier. To demonstrate this capability, we measure the HOM interference at various relative path delays [Fig. 4(b)]. At the limit of our translation stage, the interference still exhibits fringes with high visibility. We note that, in practice, the usable sensing range is limited by mechanical stability and the interference visibility. In the experiment, mechanical vibrations in the HOM interferometer can induce fluctuations in the optical path difference, leading to phase drifts in the measured HOM beating. Although the RM is continuously translated by the motorized stage in 0.1 μm increments, its specified positioning accuracy is limited to 0.3 μm, which may contribute to the observed drift. In addition, vibrations in the entangled-state preparation setup can alter the relative phase of the entangled state, further affecting the offset of the HOM beating [14]. The maximum relative path delay demonstrated here remains small compared to the meter-scale coherence length of narrowband photon pairs generated by the WGMR, and the interference visibility therefore shows no significant difference at different path delays. Nevertheless, the demonstrated optical delay already exceeds the coherence length achievable with non-resonant PDC sources, which is typically limited to a few millimeters [8].

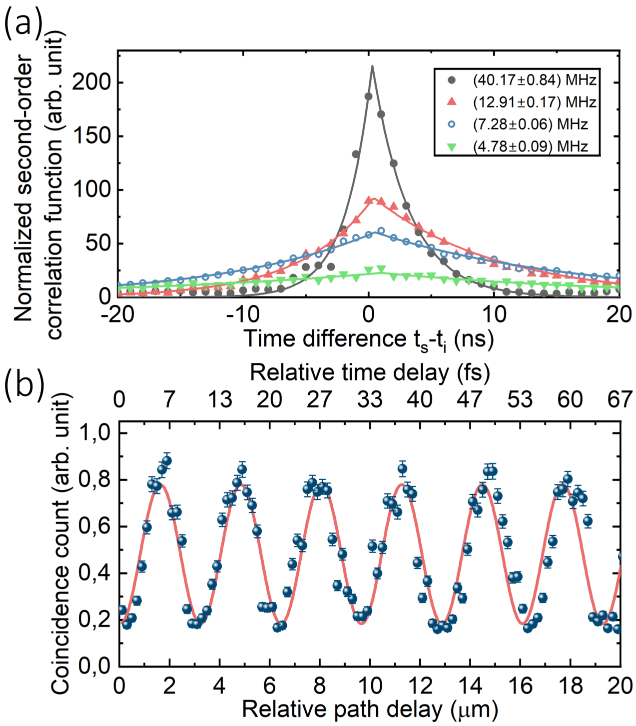

Fig. 5. (a) Normalized second-order correlation functions under various coupling conditions. (b) HOM interference measured under the overcoupling condition exhibits sinusoidal oscillations with a fitted beating period of (3.20 ± 0.01) μm and an interference visibility of (61.8 ± 3.0) %. The errors are calculated assuming Poissonian statistics for photon counting. The corresponding photon-pair bandwidth is (43.55 ± 3.63) MHz. The acquisition time for the HOM beating measurement is 1 second.

In our experimental configuration, the generated photons are evanescently coupled out of the WGMR using a diamond prism coupler. By precisely adjusting the distance between the prism and the WGMR, the coupling rate can be broadly and continuously tuned, providing an efficiently and flexible way of controlling the bandwidth of the photon pairs. When the prism is moved close to the WGMR, the coupling rate increases to exceed the internal loss rate. This overcoupling condition leads to a higher total cavity decay rate, resulting in a broader bandwidth of the emitted photon pairs. Conversely, when the prism is positioned farther from the WGMR, the coupling rate decreases, allowing photons to propagate longer within the resonator. The photon lifetime is therefore extended, leading to a lower cavity decay rate and narrower bandwidth of photon pairs. The measured Glauber correlation functions for difference coupling distances of the WGMR are shown in Fig. 5(a). The photon-pair bandwidth demonstrated can be continuously tuned from (4.78 ± 0.09) MHz to (40.17 ± 0.84) MHz. This wide tuning range shows the versatility of our WGMR-based source for applications requiring adjustable spectral properties.

To further study the influence of the coupling condition on HOM interference, we measured the HOM interference in the overcoupling regime, where the photon-pair bandwidth is broadened to (43.55 ± 3.63) MHz, as shown in Fig. 5(b). Under the higher coupling rate and broader photon-pair bandwidth, the characteristic HOM beating effect remains clearly observable. The fitted beating period is (3.20 ± 0.01) μm, which is close to the expected value of (3.134 ± 0.002) μm, and is independent of the photon-pair bandwidth.

4. DISCUSSION

The demonstrated ability to flexibly control the photon bandwidth provides an additional degree of freedom for applications requiring tunable spectral properties. For instance, the measurement resolution can be enhanced by increasing the phase accumulation time during the interaction between the sensing photon and the target system. In this context, atomic quantum memories offer a promising way to extend the interaction time and enable hybrid sensing applications [22,23]. When frequency-entangled photons interact with a quantum memory, the induced phase shifts contribute to a relative phase within the entangled state. This relative phase leads to a shift in the HOM dip and can be directly probed through HOM measurements. Efficient interfacing with such systems requires the photon bandwidth to be matched to the atomic linewidth [10]. Similarly, in applications that rely on interference between photons from multiple narrowband sources, such as quantum teleportation and entanglement swapping, their spectral properties must be carefully matched. In particular, the photon bandwidths need to be tuned to ensure optimal indistinguishability at the Bell state measurement setup, thus maximizing the interference visibility and the success probability of the protocol [21]. In addition to the tunability of the photon bandwidth, we note that the central wavelengths of the signal and idler photons generated from the WGMR can also be efficiently tuned. By adjusting the crystal temperature by only ten degree Celsius, the photon wavelengths can be tuned from a degenerate emission to a significantly non-degenerate condition with wavelength difference between the signal and idler photons exceeding 300 nm, which corresponds to a frequency detuning more than 90 THz. By further leveraging the angular phase-matching conditions in spherical geometries, photon pairs with greater nondegeneracy can be generated by selectively coupling to whispering gallery modes with higher radial mode number or cluster numbers [24]. This approach provides additional degrees of freedom for controlling the frequency detuning between the signal and idler photons, thus broadening the accessible spectral range. Moreover, the triply resonant and highly nondegenerate PDC can be easily achieved by taking advantage of the total internal reflection within the WGMR. Our compact WGMR-based narrowband photon source does not require complex reflector fabrication or intricate cavity control.

In summary, we demonstrate a narrowband frequency-entangled photon source based on a crystalline WGMR. The narrow spectral bandwidth of the photons, corresponding to a long temporal wave packet, enables a meter-scale dynamic scanning range for HOM interferometry, while the quantum beat note provides sub-picosecond resolution. This enhancement makes our photon source feasible to perform time-resolved sensing for probing the coherent transfer of entangled photons [25,26] and for precise in-fiber sensing for eavesdropper localization in optical fiber networks [6,27]. We also note that by operating the WGMR in a spectral multimode regime, where multiple narrowband frequency modes can be extracted simultaneously, our frequency-entangled photon source may have potential applications in scalable frequency-bin-encoded quantum key distribution (QKD) networks [28,29]. Implementing a ring resonator on a lithium niobate or silicon photonic integrated circuit [30,31] could further enable a more stable and compact realization of a frequency-entangled photon source. Our work therefore opens new opportunities for employing narrowband frequency-entangled photon pairs in the development of novel quantum information processing technologies.

Funding. Bundesministerium für Forschung, Technologie und Raumfahrt (16KIS1264); European Union's Horizon Europe research and innovation programme under the project "Quantum Secure Networks Partnership" (101114043).

Acknowledgment. This work was supported by European Union's Horizon Europe research and innovation programme under the project "Quantum Secure Networks Partnership" (QSNP, grant agreement No 101114043), and by the German Federal Ministry for Research, Technology and Space (BMFTR) in the context of the federal government's research framework in IT-security "Digital. Secure. Sovereign." (Project No. 16KIS1264).

Disclosures. The authors declare no conflicts of interest.

Data availability. Data underlying the results presented in this paper are not publicly available at this time but may be obtained from the authors upon reasonable request.

Supplemental document. See Supplement 1 for more detailed information.

REFERENCES

1. D. Lopez-Mago and L. Novotny, "Quantum-optical coherence tomography with collinear entangled photons," Opt. Lett. **37**, 4077–4079 (2012).
2. B. Ndagano, H. Defienne, D. Branford, *et al.*, "Quantum microscopy based on Hong–Ou–Mandel interference," Nat. Photonics **16**, 384–389 (2022).
3. A. Eshun, B. Gu, O. Varnavski, *et al.*, "Investigations of molecular optical properties using quantum light and Hong–Ou–Mandel interferometry," J. Am. Chem. Soc. **143**, 9070–9081 (2021).
4. S. Restuccia, M. Toroš, G. M. Gibson, *et al.*, "Photon bunching in a rotating reference frame," Phys. Rev. Lett. **123**, 110401 (2019).
5. Z. Y. Ou and L. Mandel, "Observation of spatial quantum beating with separated photodetectors," Phys. Rev. Lett. **61**, 54–57 (1988).
6. Y. Chen, M. Fink, F. Steinlechner, *et al.*, "Hong-Ou-Mandel interferometry on a biphoton beat note," npj Quantum Inf. **5**, 43 (2019).
7. C. Torre, A. McMillan, J. Monroy-Ruz, *et al.*, "Sub-μm axial precision depth imaging with entangled two-color Hong-Ou-Mandel microscopy," Phys. Rev. A **108**, 023726 (2023).
8. C. P. Lualdi, S. J. Johnson, M. Vayninger, *et al.*, "Fast quantum interferometry at the nanometer and attosecond scales with energy-entangled photons," Sci. Adv. **11**, eadw4938 (2025).
9. S. Ramelow, L. Ratschbacher, A. Fedrizzi, *et al.*, "Discrete tunable color entanglement," Phys. Rev. Lett. **103**, 253601 (2009).
10. S. Zhang, C. Liu, S. Zhou, *et al.*, "Coherent control of single-photon absorption and reemission in a two-level atomic ensemble," Phys. Rev. Lett. **109**, 263601 (2012).
11. C.-H. Wu, T.-Y. Wu, Y.-C. Yeh, *et al.*, "Bright single photons for light-matter interaction," Phys. Rev. A **96**, 023811 (2017).
12. A. Otterpohl, F. Sedlmeir, U. Vogl, *et al.*, "Squeezed vacuum states from a whispering gallery mode resonator," Optica **6**, 1375–1380 (2019).
13. M. Förtsch, J. U. Fürst, C. Wittmann, *et al.*, "A versatile source of single photons for quantum information processing," Nat. Commun. **4**, 1818 (2013).
14. S.-H. Huang, T. Dirmeier, G. Shafiee, *et al.*, "Polarization-entangled photons from a whispering gallery resonator," npj Quantum Inf. **10**, 85 (2024).
15. M. Mohageg, L. Mazzarella, C. Anastopoulos, *et al.*, "The deep space quantum link: prospective fundamental physics experiments using long-baseline quantum optics," EPJ Quantum Technol. **9**, 25 (2022).
16. C.-S. Chuu and S. E. Harris, "Ultrabright backward-wave biphoton source," Phys. Rev. A **83**, 061803 (2011).
17. A. Lyons, G. C. Knee, E. Bolduc, *et al.*, "Attosecond-resolution Hong-Ou-Mandel interferometry," Sci. Adv. **4**, eaap9416 (2018).
18. O. Meskine, E. Descamps, A. Keller, *et al.*, "Approaching maximal precision of Hong-Ou-Mandel interferometry with nonperfect visibility," Phys. Rev. Lett. **132**, 193603 (2024).
19. N. Fabre and S. Felicetti, "Parameter estimation of time and frequency shifts with generalized Hong-Ou-Mandel interferometry," Phys. Rev. A **104**, 022208 (2021).
20. G. Schunk, J. U. Fürst, M. Förtsch, *et al.*, "Identifying modes of large whispering-gallery mode resonators from the spectrum and emission pattern," Opt. Express **22**, 30795–30806 (2014).
21. S.-H. Huang, T. Dirmeier, G. Shafiee, *et al.*, "Indistinguishable MHz-narrow heralded photon pairs from a whispering gallery resonator," APL Photonics **10**, 056111 (2025).
22. S. Zaiser, T. Rendler, I. Jakobi, *et al.*, "Enhancing quantum sensing sensitivity by a quantum memory," Nat. Commun. **7**, 12279 (2016).
23. A. Ahmadi, Y. Murat, P.-C. Kuan, *et al.*, "Controlled displacement of stored light at room temperature," Phys. Rev. A **112**, L021501 (2025).
24. M. Förtsch, G. Schunk, J. U. Fürst, *et al.*, "Highly efficient generation of single-mode photon pairs from a crystalline whispering-gallery-mode resonator source," Phys. Rev. A **91**, 023812 (2015).
25. E. Altewischer, M. P. van Exter, and J. P. Woerdman, "Plasmon-assisted transmission of entangled photons," Nature **418**, 304–306 (2002).
26. C.-Y. Cheng, J.-H. Yang, Y.-J. Chen, *et al.*, "Time-resolved detection of photon–surface-plasmon coupling at the single-quanta level," Phys. Rev. A **102**, 033724 (2020).
27. A. Popp, F. Sedlmeir, B. Stiller, *et al.*, "Eavesdropper localization for quantum and classical channels via nonlinear scattering," Opt. Quantum **2**, 21–28 (2024).
28. A. Khodadad Kashi and M. Kues, "Frequency-bin-encoded entanglement-based quantum key distribution in a reconfigurable frequency-multiplexed network," Light Sci. Appl. **14**, 49 (2025).
29. N. Tagliavacche, M. Borghi, G. Guarda, *et al.*, "Frequency-bin entanglement-based quantum key distribution," npj Quantum Inf. **11**, 60 (2025).
30. D. Zhu, L. Shao, M. Yu, *et al.*, "Integrated photonics on thin-film lithium niobate," Adv. Opt. Photonics **13**, 242–352 (2021).
31. Y. Guo, W. Zhang, S. Dong, *et al.*, "Telecom-band degenerate-frequency photon pair generation in silicon microring cavities," Opt. Lett. **39**, 2526–2529 (2014).